energies

MDPI

Article

Adaptive Tracking Method of Distorted Voltage Using IMM Algorithm under Grid Frequency Fluctuation Conditions

Haoyao Nie [1,2] and Xiaohua Nie [3,*]

[1] School of Economics and Management, Nanchang University, Nanchang 330031, China; hynie003@outlook.com
[2] I.H. Asper School of Business, University of Manitoba, Winnipeg, MB R3T 5V4, Canada
[3] Department of Energy and Electrical Engineering, Nanchang University, Nanchang 330031, China
* Correspondence: niexiaoh@163.com

Abstract: This paper newly proposes an interactive multiple model (IMM) algorithm to adaptively track distorted AC voltage with the grid frequency fluctuation. The usual tracking methods are Kalman filter (KF) algorithm with a fixed frequency and KF algorithm with frequency identifier. The KF algorithm with a fixed frequency has a larger covariance parameter to guarantee the tracking robustness. However, it has a large tracking error. The KF algorithm with frequency identifier overly depends on the accuracy and stability of frequency identifier. The advantage of the proposed method is that it is decoupled from frequency detection and does not depend on frequency detection accuracy. First, the orthogonal vector dynamic (OVD) tracking model of the sine wave is established. Then, a model set covering the grid frequency fluctuation range is formed, and a new OVD-IMM tracking algorithm is proposed in combination with IMM algorithm. In the end, the effectiveness and accuracy of the proposed OVD-IMM algorithm are verified through simulations and experiments.

Keywords: frequency fluctuation; distorted voltage; Kalman filter; dynamic tracking model; interacting multiple model algorithm

check for updates

Citation: Nie, H.; Nie, X. Adaptive Tracking Method of Distorted Voltage Using IMM Algorithm under Grid Frequency Fluctuation Conditions. *Energies* **2021**, *14*, 7944. https://doi.org/10.3390/en14237944

Academic Editor: Muhammad Aziz

Received: 3 November 2021
Accepted: 22 November 2021
Published: 26 November 2021

Publisher's Note: MDPI stays neutral with regard to jurisdictional claims in published maps and institutional affiliations.

Copyright: © 2021 by the authors. Licensee MDPI, Basel, Switzerland. This article is an open access article distributed under the terms and conditions of the Creative Commons Attribution (CC BY) license (https://creativecommons.org/licenses/by/4.0/).

1. Introduction

The Kalman filter (KF), which is widely used in some power electronics fields, represents its advantages such as zero steady-state error, high real-time performance, better division of signal state and noise, and so on [1]. For example, it applies to the following fields such as harmonic estimation [2–8], travelling-wave fault location [9,10], waveform envelope detection of AC signals for power quality control equipment [11–17], power quality disturbance detection and classification [18–26], and synchronization control methods [27–33], and so on.

As we all know, as the source-grid-load changes, the power grid frequency is not fixed at 50 Hz but fluctuates with time. Frequency fluctuation obeys non-Gaussian distribution. Its fluctuation range generally reaches 49.5 Hz–50.5 Hz [34]. Some methods in the literature are to use the KF algorithm with a fixed frequency [27,28]. When tracking the AC voltage, the KF algorithm covariance parameter is 0.05. The parameter of 0.05 is larger and the frequency band is wider. It guarantees the robustness of the KF algorithm when the frequency fluctuates. However, it has a large tracking error. Another method uses KF algorithm with real-time frequency identifier, as shown in Figure 1 [29–33]. This kind of tracking method realizes adaptive tracking by feeding back the estimated value of the fundamental frequency. Different frequency detection algorithms are used in the literature, such as extended Kalman filter (EKF) combined with integrator estimation method [29], generalized averaging method [30], frequency locked loop (FLL) [31–33], etc. The disadvantage of the KF algorithm with frequency identifier is that it requires a large amount of calculation and high frequency accuracy. If the frequency identifier is inaccurate

or unstable, it will affect the electrical signal tracking and parameter measurement accuracy, and even cause tracking failure.

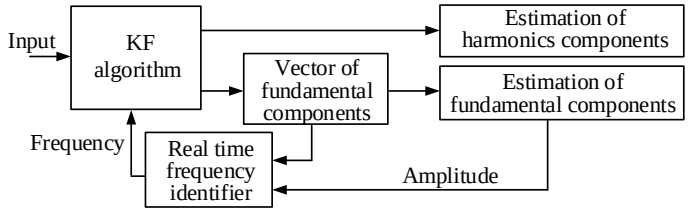

Figure 1. Tracking method based on KF algorithm with frequency identifier.

This paper presents a new method for tracking the distorted AC grid voltage of the frequency fluctuation using (interacting multiple models) IMM algorithm. It is shown in Figure 2. By comparing Figures 1 and 2, the advantage of IMM algorithm is that it does not require frequency detection and feedback tracking, and the tracking method is not affected by frequency detection accuracy and can achieve full self-adaptation. The IMM algorithm is an algorithm with Markov switching coefficients, in which multiple models of different frequencies work in parallel, and the tracking output is the result of the interaction of multiple filters [35–41]. The transfer between models is determined by Markov probability transfer matrix, which can effectively adjust the probability of each model. IMM estimates through the interaction between multiple models. Compared with the single-model algorithm, IMM is more adaptable to the fluctuation of the estimated object. It is used in hybrid control system tracking [38], maneuvering target tracking [39], human pose estimation [40], dynamic state estimation of distribution network [41], etc.

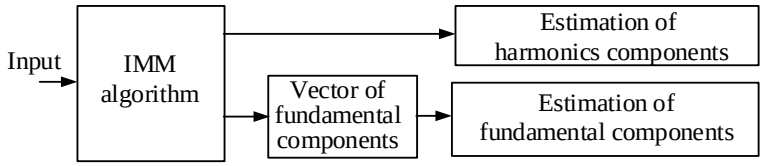

Figure 2. Proposed tracking method based on IMM algorithm.

The contributions of this paper are as follows: (a) the orthogonal vector dynamic (OVD) model is re-derived from the stochastic process theory [42], which made it clear that the covariance matrix is related to the sampling cycle. The orthogonal vector (OV) model used in conventional KF algorithm lacks theoretical derivation, and the covariance coefficient is only a fixed value of 0.05 [27,28]. The derivation of the OVD model lays the foundation for the application of the IMM algorithm. (b) The OVD-based IMM (OVD-IMM) algorithm of two models is proposed to adaptively track distorted AC grid voltage with the frequency fluctuation.

Section 1 introduces a new method for tracking the distorted AC grid voltage of the frequency fluctuation using (interacting multiple models) IMM algorithm. In Section 2, the OVD model is re-derived according to of stochastic process theory. The state space of the OVD is expanded. In Section 3, the OVD-IMM algorithm is presented and developed. In Sections 4 and 5, the performances of OVD-IMM algorithm are evaluated and compared by simulation and the experiment data. Section 6 makes a conclusion of the paper.

2. OVD Model

In Section 2, we illustrate the principle of OVD modeling. The covariance matrix of state noise for OVD model is reorganized according to the theory. The relationship between the model and the sampling cycle is clarified. We expand the state space dimension of OVD model.

2.1. Derivation of OVD Model

In two-dimensional space, the circular movement of the object along the midpoint is projected on the x, y axis as a pure sine and a pure cosine waveform, as shown in Figure 1.

It can be expressed as

$$\begin{cases} x(t) = A_m \sin(\omega_0 t + \theta) \\ y(t) = A_m \cos(\omega_0 t + \theta) \end{cases} \tag{1}$$

where, A_m is the amplitude, ω_0 is the angular frequency, and θ is the phase angle. The diagram demonstrates how the object circular movement being projected in Figure 3.

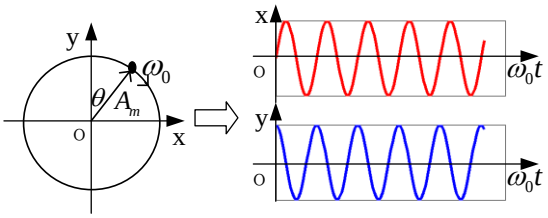

Figure 3. Diagram of the object circular movement being projected.

The first derivative can be expressed as

$$\begin{cases} \dot{x}(t) = \omega_0 A_m \cos(\omega_0 t + \theta) + w_x(t) = \omega_0 y(t) + w_x(t) \\ \dot{y}(t) = -\omega_0 A_m \sin(\omega_0 t + \theta) + w_y(t) = -\omega_0 x(t) + w_y(t) \end{cases} \tag{2}$$

where $w_x(t)$ and $w_y(t)$ are the input white noise, $w_x(t) \perp w_y(t)$. $w_x(t) \sim (0, \sigma_w^2)$, $w_y(t) \sim (0, \sigma_w^2)$.

The state equation can be obtained from (1).

$$\frac{d}{dt}\begin{bmatrix} x(t) \\ y(t) \end{bmatrix} = A\begin{bmatrix} x(t) \\ y(t) \end{bmatrix} + B\begin{bmatrix} w_x(t) \\ w_y(t) \end{bmatrix} \tag{3}$$

where

$$A = \begin{bmatrix} 0 & \omega_0 \\ -\omega_0 & 0 \end{bmatrix}, \; B = \begin{bmatrix} 1 & 0 \\ 0 & 1 \end{bmatrix}$$

Equation (3) is discretized, and we get the state equation as follows

$$\begin{bmatrix} x \\ y \end{bmatrix}_{k+1} = \Phi_k \begin{bmatrix} x \\ y \end{bmatrix}_k + W_k \tag{4}$$

where

$$\Phi_k = e^{AT} = L^{-1}([sI - A]^{-1}) = \begin{bmatrix} \cos(\omega_0 T) & \sin(\omega_0 T) \\ -\sin(\omega_0 T) & \cos(\omega_0 T) \end{bmatrix} \tag{5}$$

$$W_k = \int_{kT}^{(k+1)T} e^{A[(k+1)T-\tau]} \cdot B \cdot w(\tau) d\tau \tag{6}$$

The covariance matrix of state noise W_k can be expressed as

$$Q_k = E\left[W_k W_k^T\right] = \sigma_w^2 \begin{bmatrix} T & 0 \\ 0 & T \end{bmatrix} = \sigma_w^2 T \begin{bmatrix} 1 & 0 \\ 0 & 1 \end{bmatrix} \tag{7}$$

From Equation (7), an important conclusion can be known that Q_k is related to sampling cycle T.

2.2. Dimension Expansion of OVD Model

The waveform of the distorted AC signal sampled at time t would be presented as

$$s(t) = \sum_{i=1}^{N} A_i(t) \sin[i\omega T + \theta_i(t)] + \sum_{i=1}^{N} w_i(t) \tag{8}$$

where $i = 1, 2, 3, \cdots, N$ represents the number of fundamental and harmonic components, T is the sampling cycle. The fundamental frequency is $\omega = 100\pi \pm \mathrm{e}$, while e is the frequency fluctuation value. $\sum_{i=1}^{N} A_i(t) \sin[i\omega T + \theta_i(t)]$ and $\sum_{i=1}^{N} w_i(t)$ represent the fundamental and harmonic components, and their state noise, respectively.

For Equation (1), the dimensionality of the OVD model is expanded under the consideration of fundamental and harmonic components.

$$X(t) = \begin{bmatrix} x_1(t) & y_1(t) & x_2(t) & y_2(t) & \cdots & \mathrm{x}_n(t) & y_n(t) \end{bmatrix}^T \tag{9}$$

where $y_i(t)$ is the orthogonality of $x_i(t)$. In the condition of continuous time, the state space expression is established.

$$\frac{dX(t)}{dt} = \begin{bmatrix} M_1 & 0 & \cdots & 0 \\ 0 & M_2 & 0 & \vdots \\ \vdots & 0 & \ddots & 0 \\ 0 & \cdots & 0 & M_n \end{bmatrix} X(t) + \begin{bmatrix} w_1(t) \\ w_2(t) \\ \vdots \\ w_n(t) \end{bmatrix} \tag{10}$$

where the state noise vector is $\begin{bmatrix} w_1(t) & w_2(t) & \cdots & w_n(t) \end{bmatrix}^T$.

$$M_1 = \begin{bmatrix} 0 & \omega_m \\ -\omega_m & 0 \end{bmatrix}, M_2 = \begin{bmatrix} 0 & 3 \times \omega_m \\ -3 \times \omega_m & 0 \end{bmatrix}, M_n = \begin{bmatrix} 0 & \mathrm{i} \times \omega_m \\ -\mathrm{i} \times \omega_m & 0 \end{bmatrix}.$$

where ω_m represents the fixed frequency of this model, different values of ω_m represent different models.

The measurement equation is

$$z(t) = \begin{bmatrix} 1 & 0 & 1 & 0 & \cdots & 1 & 0 \end{bmatrix} X(t) + v(t) \tag{11}$$

where the measurement noise vector is $v(t)$.

We discretize Equations (10) and (11) in accordance with the principle of OVD model. Then, the state and measurement equation can be

$$\begin{cases} X_{k+1} = \begin{bmatrix} \Phi_1 & \cdots & 0 \\ \vdots & \cdots & \vdots \\ 0 & \cdots & \Phi_n \end{bmatrix} X_k + + \begin{bmatrix} W_1 \\ W_2 \\ \vdots \\ W_n \end{bmatrix} \\ z_k = H_k X_k + V_k \end{cases} \tag{12}$$

where $X_k = \begin{bmatrix} x_{1k} & y_{1k} & x_{2k} & y_{2k} & \cdots & x_{nk} & y_{nk} \end{bmatrix}^T$, $\begin{bmatrix} W_1 & W_2 & \cdots & W_n \end{bmatrix}_k^T$ is the state noise. The state transition matrixes and the measurement transfer matrix are shown below as

$$\Phi_i = \begin{bmatrix} \cos(i\omega_m T) & \sin(i\omega_m T) \\ -\sin(i\omega_m T) & \cos(i\omega_m T) \end{bmatrix} \tag{13}$$

$$H_k = \begin{bmatrix} 1 & 0 & 1 & 0 & \cdots & 1 & 0 \end{bmatrix} \tag{14}$$

The covariance matrix of state noise W_{k_i} is

$$Q_{i_k} = E\left[W_{i_k} {W_{i_k}}^T\right] = \sigma_{OV}^2 T I_{2n\times 2n} \tag{15}$$

The difference from the traditional *OV* model in the [27,28] is that Q is different. The OVD model clarifies the relationship between the covariance matrix and the sampling cycle. The IMM algorithm cannot just adopt the traditional *OV* model's covariance coefficient of 0.05. Otherwise, the IMM algorithm will bring tracking errors.

If we just choose the fixed value of 0.05, when the frequency fluctuates, the traditional *OV* algorithm still adjusts the amplification factor K according to the covariance Q of the fixed frequency. The lack of dynamic tracking performance results in the algorithm not being able to track the dynamic fluctuations in time. The IMM algorithm uses maximum likelihood estimation to determine the transition probability between models to adaptive tracking dynamic fluctuations. Therefore, the IMM algorithm has stronger and more stable adaptive tracking capability.

3. OVD Model-Based IMM Algorithm

In this section, the OVD Model-based IMM Algorithm (OVD-IMM) is proposed by combining OVD models and IMM algorithm. Then, the parameters of two model OVD-IMM algorithms are selected.

3.1. OVD-IMM Algorithm

The block diagram of IMM Algorithm is presented in Figure 4. The IMM algorithm formula is shown in Table 1.

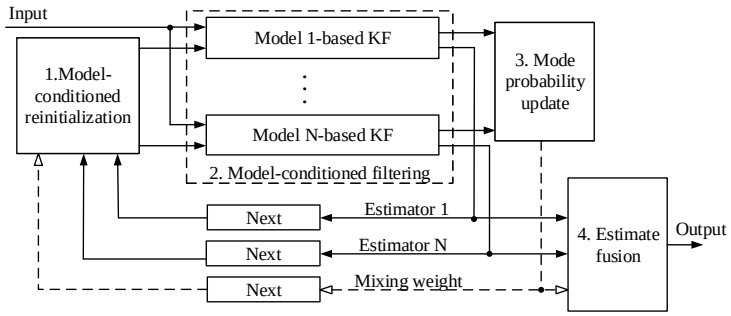

Figure 4. Block diagram of IMM Algorithm.

In the Table 1, j represents the number of different models, π_{ji} and $\mu_{k-1}^{(j)}$ denote the initial given values of mode probability and mixing weight, respectively. $\hat{\mathbf{X}}_{k|k}^{(i)}$ and $\mathbf{P}_{k|k}^{(i)}$ represent state estimate of filter i at k and its covariance. $\overline{\mathbf{X}}_{k|k}^{(i)}$ and $\overline{\mathbf{P}}_{k|k}^{(i)}$ denote mixed conditions for filter i at time k. $\hat{\mathbf{X}}_{k+1|k+1}$ and $\mathbf{P}_{k+1|k+1}$ indicate combined state estimate and its covariance. $\mu_k^{(i)}$ is mode probability at time k. $\mu_k^{j|i}$ is mixing probability at time k. $\mathbf{L}_k^{(i)}$ expresses the likelihood function of filter i.

Multiple models with different frequencies ω_m in (12) and (13) form a model set, and substituting them into formula Table 1 to form the OVD Model-based IMM (OVD-IMM) algorithm.

Table 1. One cycle of IMM algorithm.

(1). Model-Conditioned Reinitialization (for i = 1,2, . . . ,N):
Predicted mode probability:
Mixing weight: $\mu_k^{j\|i} \triangleq \mathbf{P}\left\{\mathbf{m}_k^{(j)} \middle\| \mathbf{m}_k^{(i)}, \mathbf{Z}^{k-1}\right\} = \pi_{ji}\mu_{k-1}^{(j)} / \mu_{k\|k-1}^{(i)}$
Mixing estimate: $\overline{\mathbf{X}}_{k\|k}^{(i)} \triangleq E\left[\mathbf{X}_k \middle\| \mathbf{m}_k^{(i)}, Z^k\right] = \sum_j \hat{\mathbf{X}}_{k\|k}^{(j)} \mu_k^{j\|i}$
Mixing covariance: $\overline{\mathbf{P}}_{k\|k}^{(i)} = \sum_j \left[\mathbf{P}_{k\|k}^{(j)} + (\overline{\mathbf{X}}_{k\|k}^{(i)} - \hat{\mathbf{X}}_{k\|k}^{(j)})(\overline{\mathbf{X}}_{k\|k}^{(i)} - \hat{\mathbf{X}}_{k\|k}^{(j)})'\right] \mu_k^{j\|i}$
(2). Model-Conditioned Filtering (for i = 1,2):
Predicted state: $\hat{\mathbf{X}}_{k+1\|k}^{(i)} = \Phi_k^{(i)} \overline{\mathbf{X}}_{k\|k}^{(i)}$
Predicted covariance: $\mathbf{P}_{k+1\|k}^{(i)} = \Phi_k^{(i)} \mathbf{P}_{k\|k} (\Phi_k^{(i)})' + \mathbf{Q}_k^{(i)}$
Measurement residual: $\widetilde{\mathbf{Z}}_k^{(i)} = \mathbf{Z}_k - \mathbf{H}_k^{(i)} \hat{\mathbf{X}}_{k+1\|k}^{(i)}$
Residual covariance: $\mathbf{S}_k^{(i)} = \mathbf{H}_k^{(i)} \mathbf{P}_{k+1\|k} (\mathbf{H}_k^{(i)})' + \mathbf{R}_k$
Filter gain: $\mathbf{K}_{k+1}^{(i)} = \mathbf{P}_{k+1\|k}^{(i)} (\mathbf{H}_k^{(i)})' (\mathbf{S}_k^{(i)})^{-1}$
Updated state: $\hat{\mathbf{X}}_{k+1\|k+1}^{(i)} = \hat{\mathbf{X}}_{k+1\|k}^{(i)} + \mathbf{K}_{k+1}^{(i)} \widetilde{\mathbf{Z}}_k^{(i)}$
Updated covariance: $\mathbf{P}_{k+1\|k+1}^{(i)} = \mathbf{P}_{k+1\|k}^{(i)} - \mathbf{K}_{k+1}^{(i)} \mathbf{S}_k^{(i)} (\mathbf{K}_{k+1}^{(i)})'$
(3). Mode Probability Update (for i = 1,2, . . . ,N):
Model likelihood: $\mathbf{L}_k^{(i)} \triangleq p\left[\widetilde{\mathbf{Z}}_k^{(i)} \middle\| \mathbf{m}_k^{(i)}, \mathbf{Z}^k\right] \overset{assume}{=} N(\widetilde{\mathbf{Z}}_k^{(i)}; 0, \mathbf{S}_k^{(i)})$
Mode probability: $\mu_k^{(i)} = \frac{\mu_{k\|k-1}^{(i)} \mathbf{L}_k^{(i)}}{\sum_j \mu_{k\|k-1}^{(j)} \mathbf{L}_k^{(j)}}$
(4). Estimate Fusion:
Overall estimate: $\hat{\mathbf{X}}_{k+1\|k+1} = \sum_i \hat{\mathbf{X}}_{k+1\|k+1}^{(i)} \mu_k^{(j)}$
Overall covariance: $\mathbf{P}_{k+1\|k+1} = \sum_i \left[\mathbf{P}_{k+1\|k+1}^{(i)} + (\hat{\mathbf{X}}_{k+1\|k+1} - \hat{\mathbf{X}}_{k+1\|k+1}^{(i)})(\hat{\mathbf{X}}_{k+1\|k+1} - \hat{\mathbf{X}}_{k+1\|k+1}^{(i)})'\right] \mu_k^{(i)}$

3.2. OVD-IMM Application Development

When the IMM algorithm is applied to AC signal dynamic tracking, in order to obtain the best tracking effect, a model set that covers the frequency fluctuation mode range as much as possible must be used. However, increasing the number of models in the model set will not only increase the computational complexity, but may not necessarily improve the tracking performance. This is because an overly refined pattern space may destroy the completeness of Bayesian inference and the independence between models. Unnecessary competition from too many models will cause algorithm performance degradation.

Therefore, two frequency models covering the upper and lower limits of frequency fluctuations are adopted as a model set in this paper. The frequency of the lower limit model is $f_1 = 48.5$ Hz, the angular frequency $\omega_{m_1} = 2\pi \times f_1 = 2\pi \times 48.5$ rad/s. The frequency of the upper limit model is $f_2 = 51.5$ Hz, the angular frequency $\omega_{m_2} = 2\pi \times f_2 = 2\pi \times 51.5$ rad/s.

We calculate the amplitude and the phase angle.

$$U_{i_{k+1}} = \sqrt{\hat{x}_{i_{k+1}}^2 + \hat{y}_{i_{k+1}}^2} \tag{16}$$

$$\phi_{i_{k+1}} = \arctan\left(\frac{\hat{x}_{i_{k+1}}}{\hat{y}_{i_{k+1}}}\right) \tag{17}$$

where i = 1 is the fundamental components, i = 2,3,4, . . . is the harmonic components. $\hat{x}_{i_{k+1}}$,$\hat{y}_{i_{k+1}}$ is the fundamental components of the overall estimator in Table 1(4).

The harmonics ratio for voltage (HRU) is defined as follow

$$\mathrm{HRU_n} = \frac{U_n}{U_1} \times 100\% \tag{18}$$

where U_1 is rms value of voltage fundamental components, U_n is rms value of n-th voltage harmonic components.

4. Simulation and Evaluation

In Section 4, a fixed frequency 50 Hz model is selected to form the KF algorithm as a comparison mark to better illustrate the tracking results. We evaluate and compare OVD-IMM and KF algorithms by simulations. The HRU serves as a statistical indicator. The root means squared error (RMSE) values are adopted as statistical indicators for evaluation. At first, we set the setting of simulation. Then the tracking results of simulation data are shown in Section 4.2. Next to it, we obtain RMSE results of simulation data.

4.1. Simulation Setting

The distorted AC voltage signal formula with harmonics components is

$$\mathrm{u}(t) = 220\sqrt{2} \times [1.0\sin(\omega t) + 0.05\sin(3\omega t) + 0.1\sin(5\omega t) + 0.08\sin(7\omega t)] + 3.11v(\mathrm{t}) \quad (19)$$

The amplitude is $220\sqrt{2}$ V. The percentages of harmonic components are 5% of 3rd, 10% of 5th, and 8% of 7th. The measurement white noise is $\sigma_v = 0.01 \times 220\sqrt{2}$ V $= 3.11$ V. The sampling cycle is 0.00004 s. $\omega = 2 \times \pi \times f$ is variable. The simulation scene is divided into four situations in the condition of voltage frequency heavy fluctuations: (a) Frequency is 49.5 Hz; (b) Frequency is 50.5 Hz; (c) Frequency swell from 49.5 Hz to 50.5 Hz; (d) Frequency sag from 50.5 Hz to 49.5 Hz. The simulation voltage situations are shown in Figure 5 which includes the voltages, frequency and spectrogram of data. The simulation scene is divided into four situations in the condition of voltage frequency slight fluctuations: (a) Frequency is 49.98 Hz; (b) Frequency is 50.02 Hz; (c) Frequency swell from 49.98 Hz to 50.02 Hz; (d) Frequency sag from 50.02 Hz to 49.98 Hz. The simulation voltage situations are shown in Figure 6.

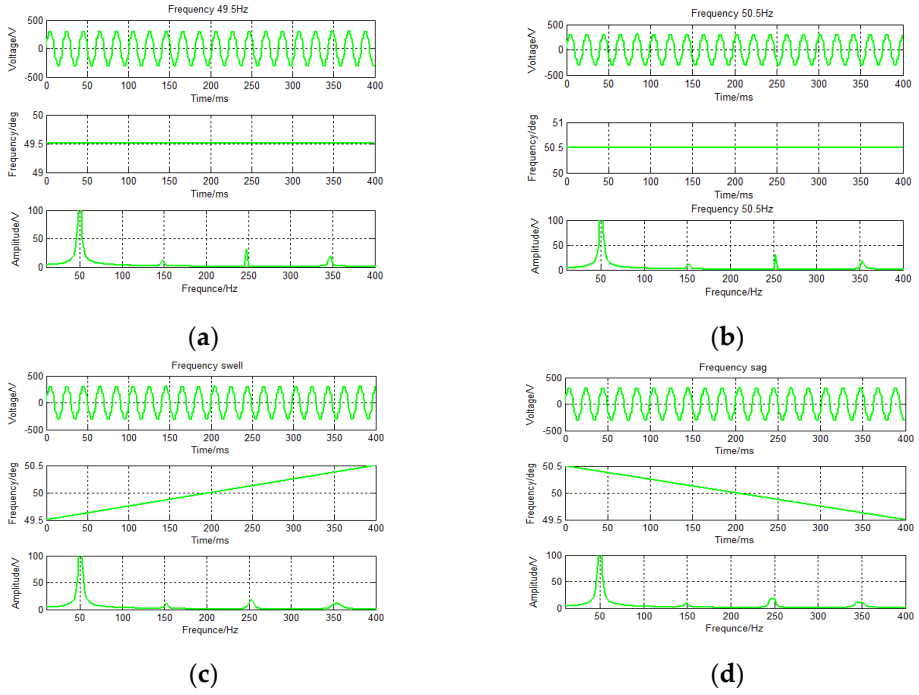

Figure 5. Simulation data for voltage frequency heavy fluctuations. (**a**) Frequency 49.5 Hz; (**b**) Frequency 50.5 Hz; (**c**) Frequency swell; (**d**) Frequency sag.

The parameters of the two algorithms are selected as follows. The R of the two algorithms is 3.11 V. The initial covariance matrices of two algorithms are employed as $P_{0/0} = 1000 \times I_{10\times10}$.

KF algorithms: the covariance of fundamental and harmonics components are all $Q_i = 0.05 \times I_{10\times10}$, like [27,28]. The covariance Q array of KF is larger and the frequency band is wider.

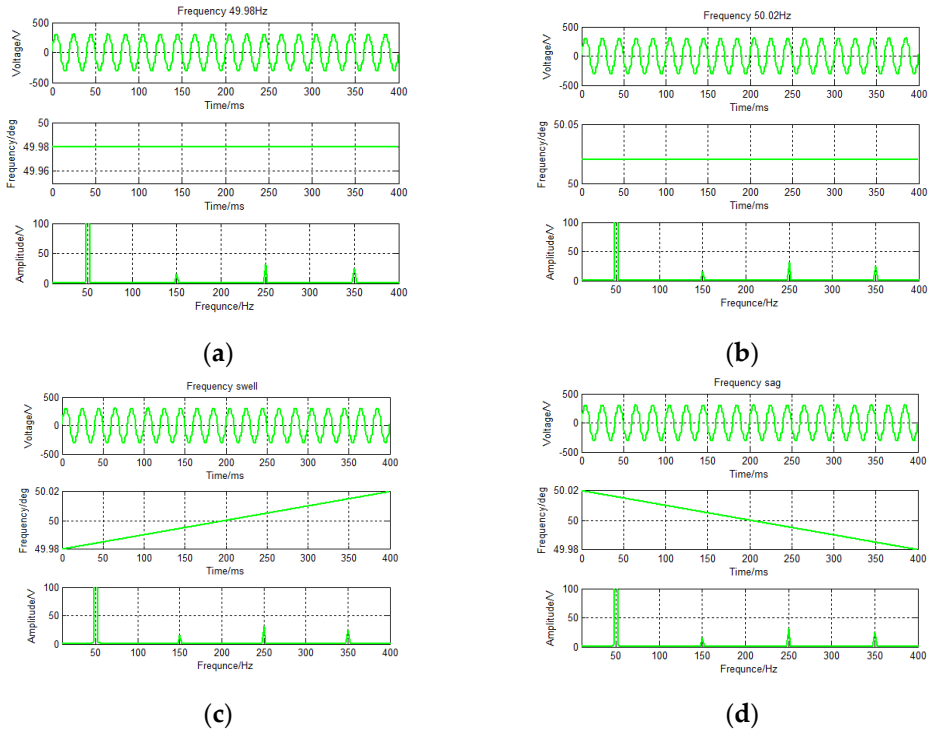

Figure 6. Simulation data for voltage frequency slight fluctuations. (**a**) Frequency 49.98 Hz; (**b**) Frequency 50.02 Hz; (**c**) Frequency swell; (**d**) Frequency sag.

IMM algorithms: The initial given values of mode probability and mixing weight, respectively, are: $\pi_{ji} = \begin{bmatrix} 0.98 & 0.02 \\ 0.02 & 0.98 \end{bmatrix}$, $\mu_{k-1}^{(1)} = 0.5$ $\mu_{k-1}^{(2)} = 0.5$. The covariance matrix of the two models is: $Q_{i_k} = \sigma_{OV}^2 T = 10 \times T \times I_{10\times10} = 0.0004 \times I_{10\times10}$. In the condition of voltage frequency heavy fluctuations, the frequencies of the two models are $\omega_{m_1} = 2\pi \times 48.5$ rad/s, $\omega_{m_2} = 2\pi \times 51.5$ rad/s. And in the condition of voltage frequency slight fluctuations, the frequencies of the two models are $\omega_{m_1} = 2\pi \times 49.85$ rad/s, $\omega_{m_2} = 2\pi \times 50.15$ rad/s.

4.2. Tracking Results of Simulation Data

The simulation tracking results of two algorithms for heavy and slight fluctuations are shown in Figures 7 and 8. The tracking results include fundamental and harmonics components.

It can be seen from Figures 7 and 8 that the IMM algorithm is stable and accurate in tracking no matter the fundamental wave or harmonic elements, and is not affected by frequency fluctuations. In Figures 7c,d and 8c,d, the accuracy of fundamental wave amplitude and harmonic tracking results is more obvious. Although the Q matrix of KF is large (0.05) and robust, the frequency mismatch also brings large tracking errors.

In order to quantitatively analyze the tracking results, the RMSE tracking results are evaluated at Section 4.3.

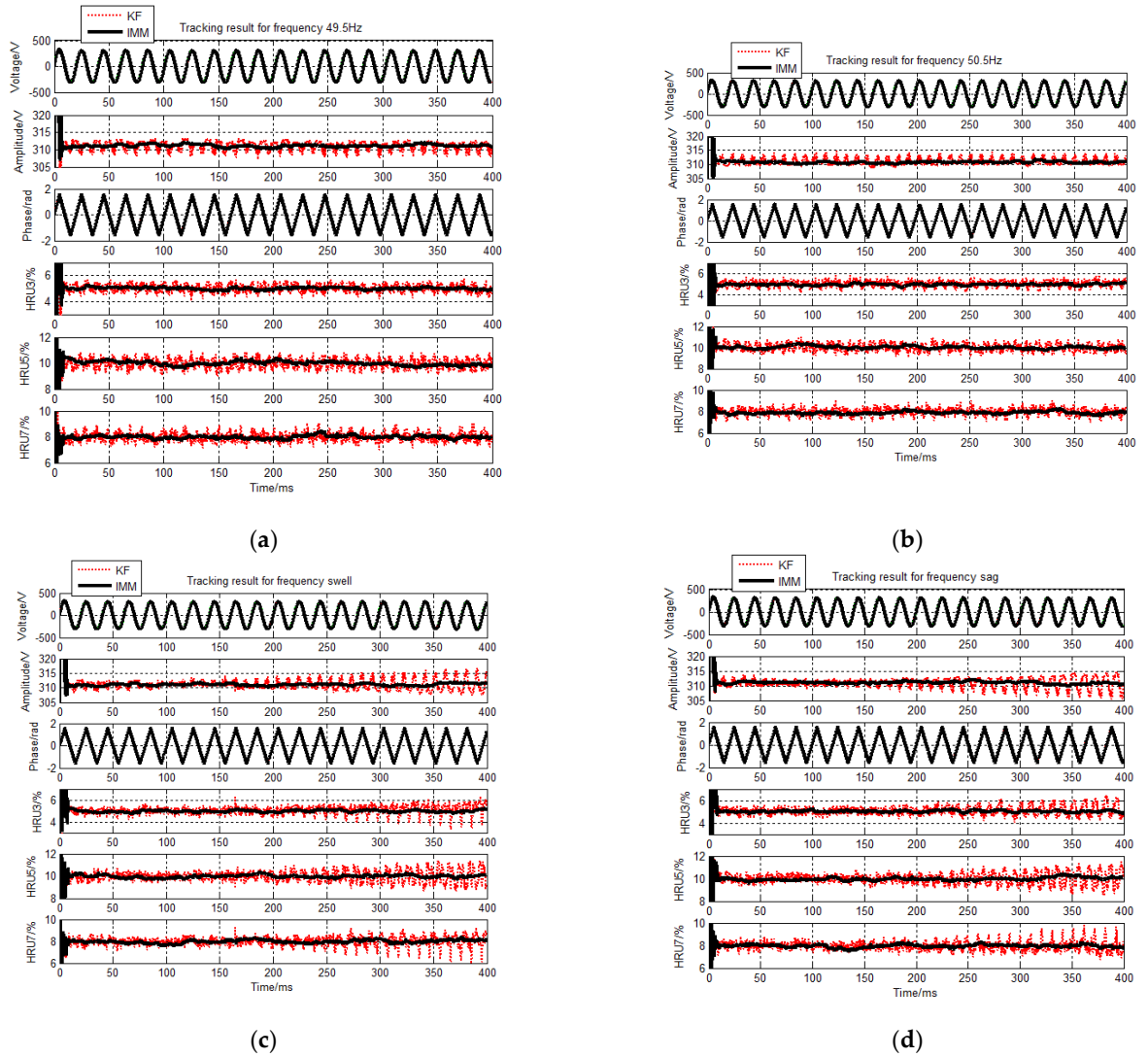

Figure 7. Simulation tracking results for voltage frequency heavy fluctuations. (**a**) Simulation tracking results for frequency 49.5 Hz; (**b**) Simulation tracking results for frequency 50.5 Hz; (**c**) Simulation tracking results for frequency swell; (**d**) Simulation tracking results for frequency sag.

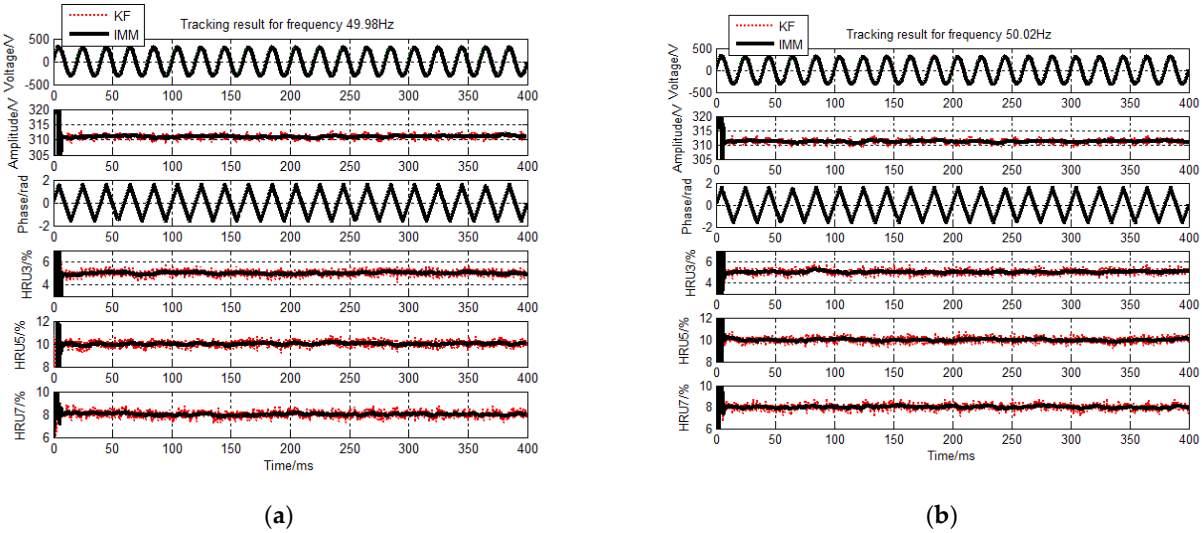

Figure 8. *Cont*.

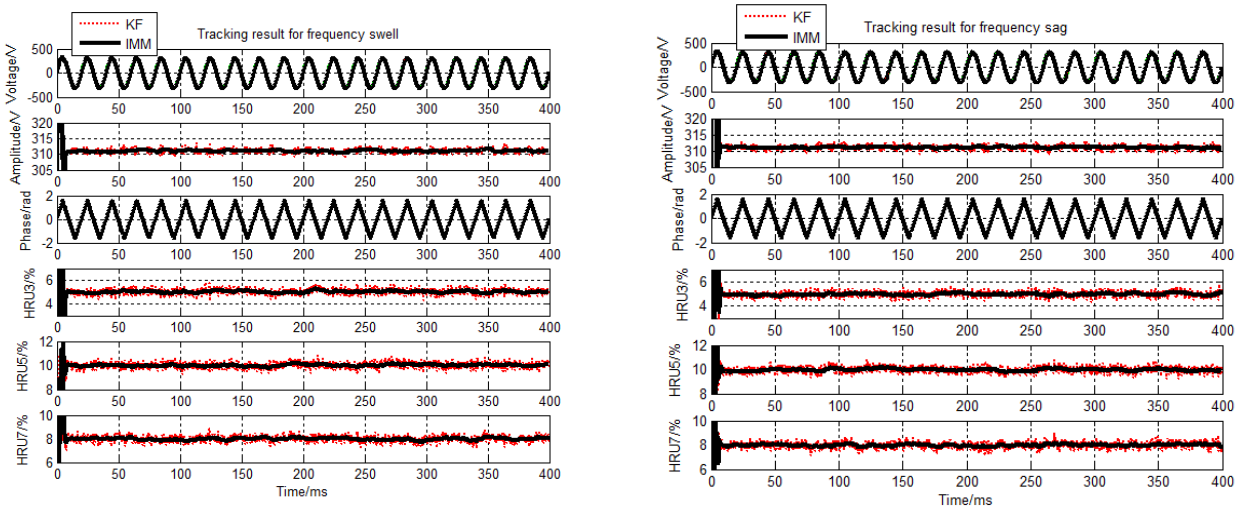

(**c**) (**d**)

Figure 8. Simulation tracking results for voltage frequency slight fluctuations. (**a**) Simulation tracking results for frequency 49.98 Hz; (**b**) Simulation tracking results for frequency 50.02 Hz; (**c**) Simulation tracking results for frequency swell; (**d**) Simulation tracking results for frequency sag.

4.3. RMSE Results of Simulation Data

The RMSE results of two algorithms calculated by 100 times Monte Carlo simulations are shown in Figures 9 and 10. The RMSE evaluation results are shown in Tables 2 and 3.

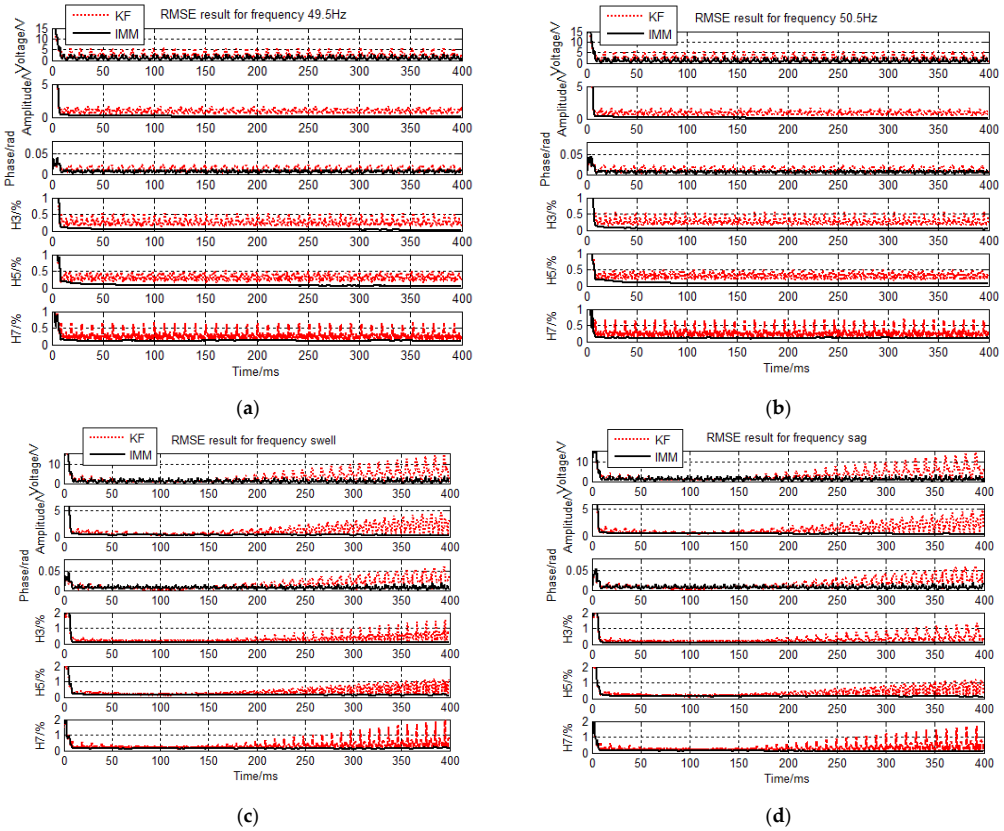

(**a**) (**b**)

(**c**) (**d**)

Figure 9. Simulation RMSE results for voltage frequency heavy fluctuations. (**a**) Simulation RMSE results for frequency 49.5 Hz; (**b**) Simulation RMSE results for frequency 50.5 Hz; (**c**) Simulation RMSE results for frequency swell; (**d**) Simulation RMSE results for frequency sag.

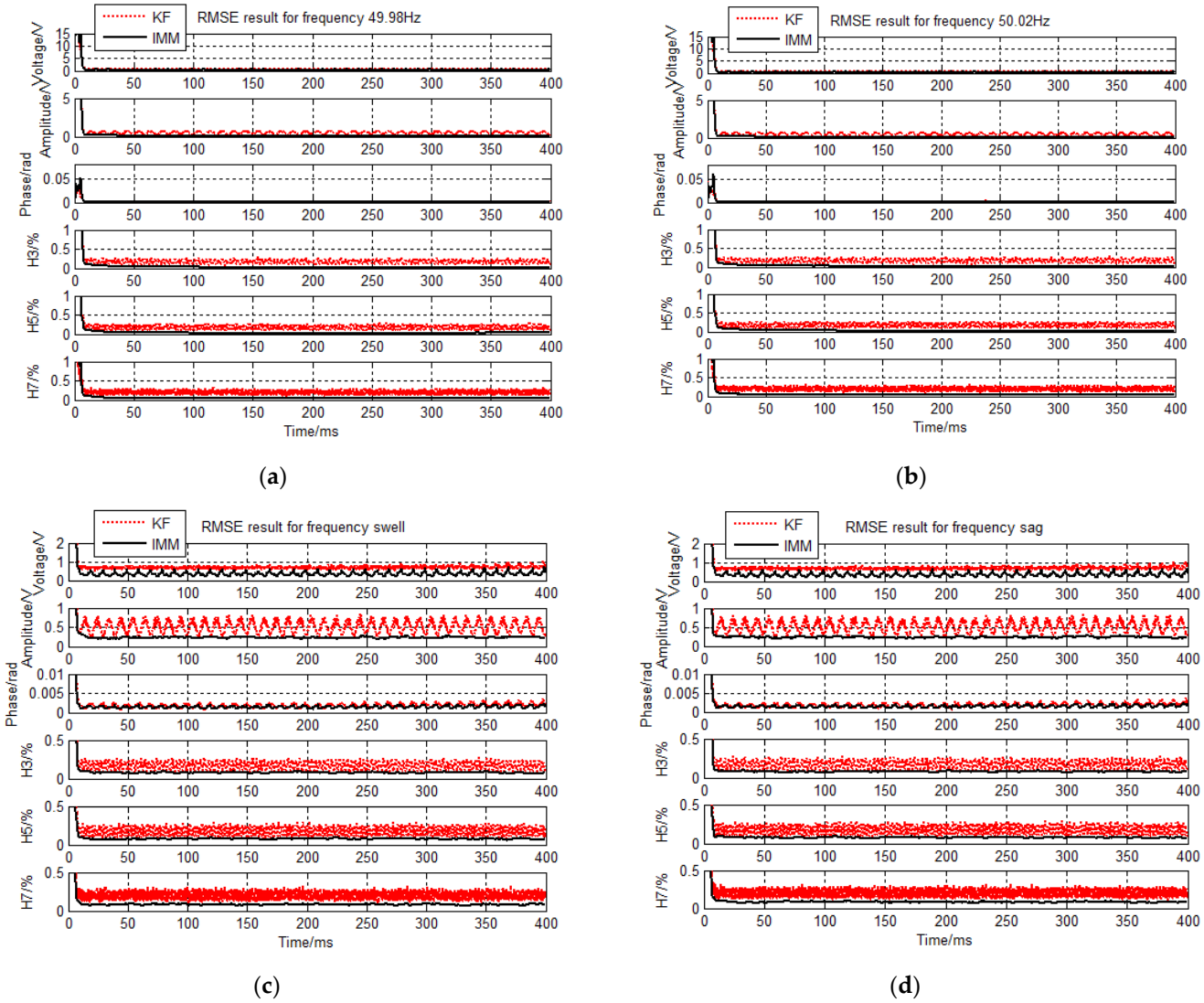

Figure 10. Simulation RMSE results for voltage frequency slight fluctuations. (**a**) RMSE results for frequency 49.98 Hz; (**b**) RMSE results for frequency 50.02 Hz; (**c**) RMSE results for frequency swell; (**d**) RMSE results for frequency sag.

Table 2. Simulation RMSE results for voltage frequency heavy fluctuations.

RMSE Results	Algorithm	Fundament Components			Harmonics Percentage		
		Signal (V)	Amplitude (V)	Phase (rad)	H3(%)	H5(%)	H7(%)
For frequency 49.5 Hz	KF	2.529610	0.930434	0.013386	0.262471	0.321099	0.264858
	IMM	1.115229	0.133475	0.006329	0.036968	0.070394	0.113563
For frequency 50.5 Hz	KF	2.543798	0.927858	0.013379	0.265402	0.322606	0.265622
	IMM	1.083361	0.151082	0.006080	0.040636	0.082606	0.108595
For frequency heavy swell	KF	3.184890	1.280741	0.016615	0.316734	0.396949	0.322599
	IMM	1.195442	0.365717	0.006781	0.092354	0.134780	0.134131
For frequency heavy sag	KF	3.152684	1.305744	0.016655	0.311159	0.400138	0.317231
	IMM	1.191125	0.358193	0.006817	0.091209	0.133590	0.115558

Table 3. Simulation RMSE results for voltage frequency slight fluctuations.

RMSE Results	Algorithm	Fundament Components			Harmonics Percentage		
		Signal (V)	Amplitude (V)	Phase (rad)	H3(%)	H5(%)	H7(%)
For frequency 49.98 Hz	KF	0.689969	0.509250	0.001745	0.167712	0.175642	0.199795
	IMM	0.296261	0.077288	0.001520	0.025432	0.030511	0.045718
For frequency 50.02 Hz	KF	0.688949	0.509281	0.001740	0.166633	0.175272	0.199700
	IMM	0.298582	0.087145	0.001518	0.025742	0.029914	0.044236
For frequency slight swell	KF	0.699127	0.512277	0.001827	0.167790	0.176890	0.199611
	IMM	0.350197	0.236394	0.001407	0.078400	0.077815	0.082226
For frequency slight sag	KF	0.701157	0.512460	0.001848	0.167786	0.176098	0.199778
	IMM	0.355450	0.237113	0.001442	0.078504	0.076419	0.083001

RMSE is defined as follows

$$\mathrm{RMSE} = \sqrt{\frac{1}{N}\sum_{k=1}^{N}\left(x_{ij} - \hat{x}_{ij}^{k}\right)^2} \tag{20}$$

where $N = 100$ is the number of simulations, x_{ij} is j-sampled values of x_i and $\hat{x}_{ij}$ j-sampled values of $\hat{x}_i$.

From Figures 9 and 10, the simulation tracking results of the IMM algorithm are stable and accurate. The KF algorithm has a large error. Especially after 200 ms, the KF algorithm has large errors in both the fundamental and the harmonics components, while the IMM algorithm is not affected.

From Table 2 to Table 3, we know that the IMM algorithm is better than the KF algorithm whether tracking results are fundamental components or harmonic components.

5. Experiment and Evaluation

In Section 5, we employ experiment data to evaluate and compare two algorithms. At the beginning, we introduce the experiment settings. Secondly, we compare tracking results of experiment sampling data for voltage frequency heavy and slight fluctuations.

5.1. Experiment Settings

The experiment platform is introduced in Figure 11a. It includes the programmable power supply and the oscilloscope. The schematic diagram of the programmable power supply is introduced in Figure 11b. Experiment data for voltage frequency heavy and slight fluctuations is conducted through a programmable power supply. The percentages of harmonic components are 5% of 3rd, 10% of 5th, and 8% of 7th. The oscilloscope of Tektronix GDS-2102 serves to sample the experiment voltage data.

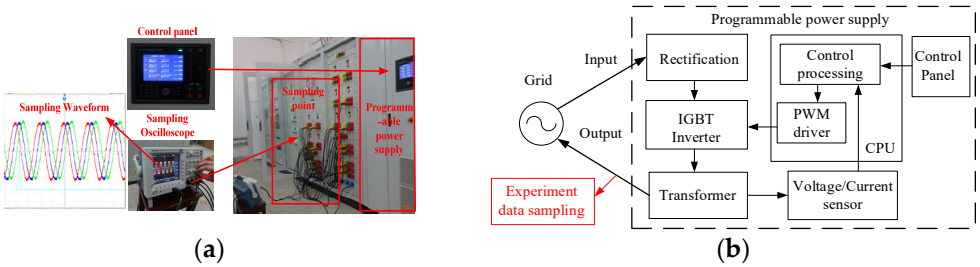

(**a**) (**b**)

Figure 11. Experiment platform and Schematic diagram. (**a**) Experiment platform. (**b**) Schematic diagram of the programmable power supply.

The sampling cycle is selected to be 0.00004 s. The experiment sampling voltage situations are shown in Figures 12 and 13.

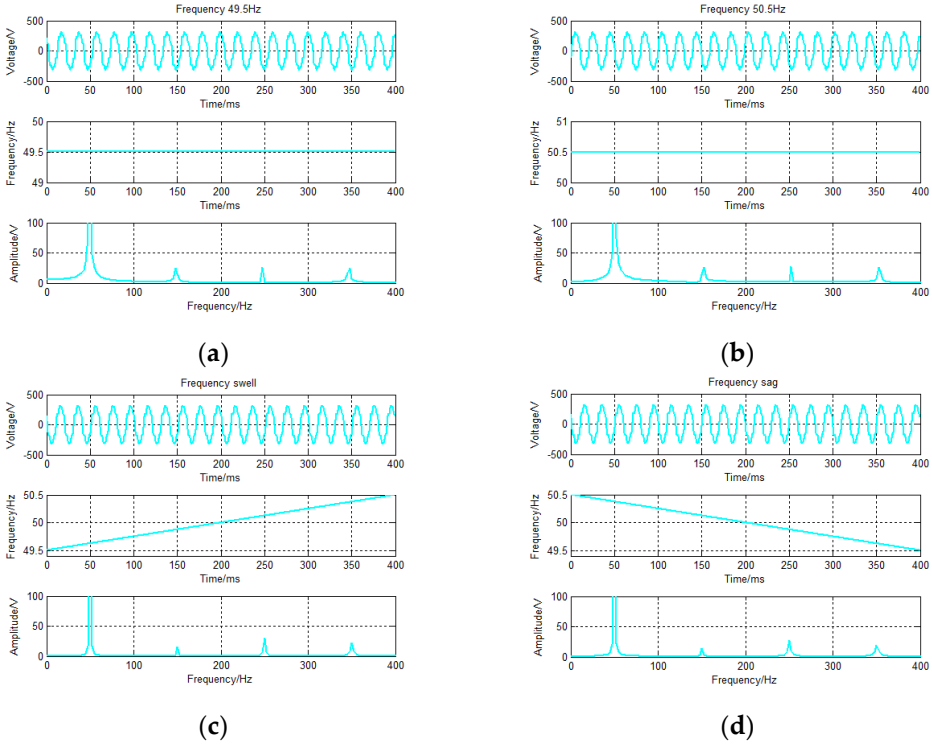

Figure 12. Experiment data for voltage frequency heavy fluctuations. (**a**) Frequency 49.5 Hz; (**b**) Frequency 50.5 Hz; (**c**) Frequency swell; (**d**) Frequency sag.

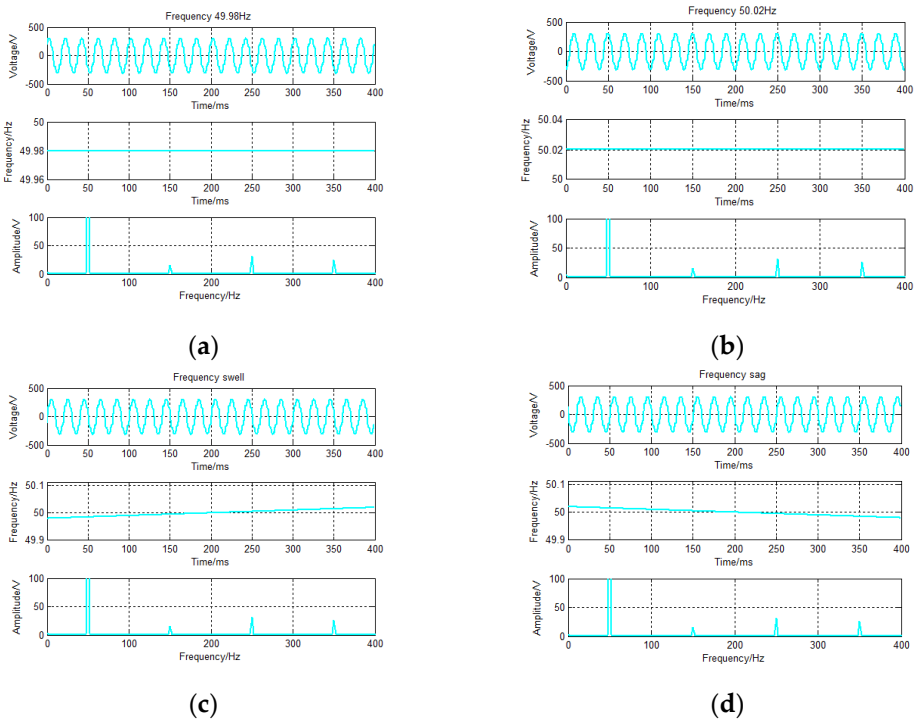

Figure 13. Experiment data for voltage frequency slight fluctuations. (**a**) Frequency 49.98 Hz; (**b**) Frequency 50.02 Hz; (**c**) Frequency swell; (**d**) Frequency sag.

5.2. Tracking Results of Experiment Sampling Data

The model parameters of the two algorithms are the same as that of the simulation evaluation in Section 4. The experiment tracking results of voltage frequency heavy and slight fluctuations are shown in Figures 14 and 15.

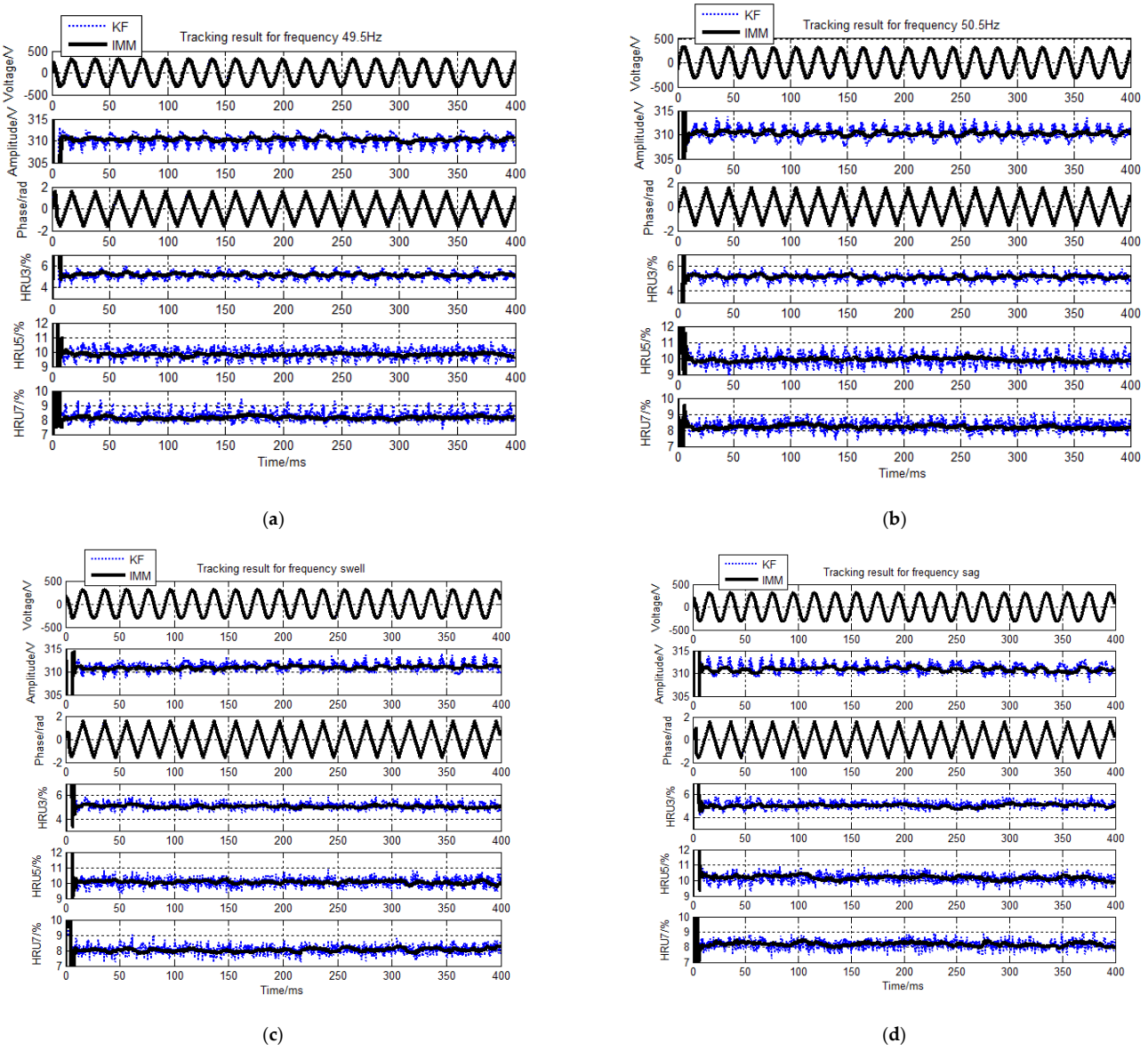

Figure 14. Experiment tracking results for voltage frequency heavy fluctuations. (**a**) Experiment tracking results for frequency 49.5 Hz; (**b**) Experiment tracking results for frequency 50.5 Hz; (**c**) Experiment tracking results for frequency swell; (**d**) Experiment tracking results for frequency sag.

From comparison results in Figures 14 and 15, the IMM algorithm is significantly better than the KF algorithm in the estimation. It is consistent with the simulation tracking results and conclusions.

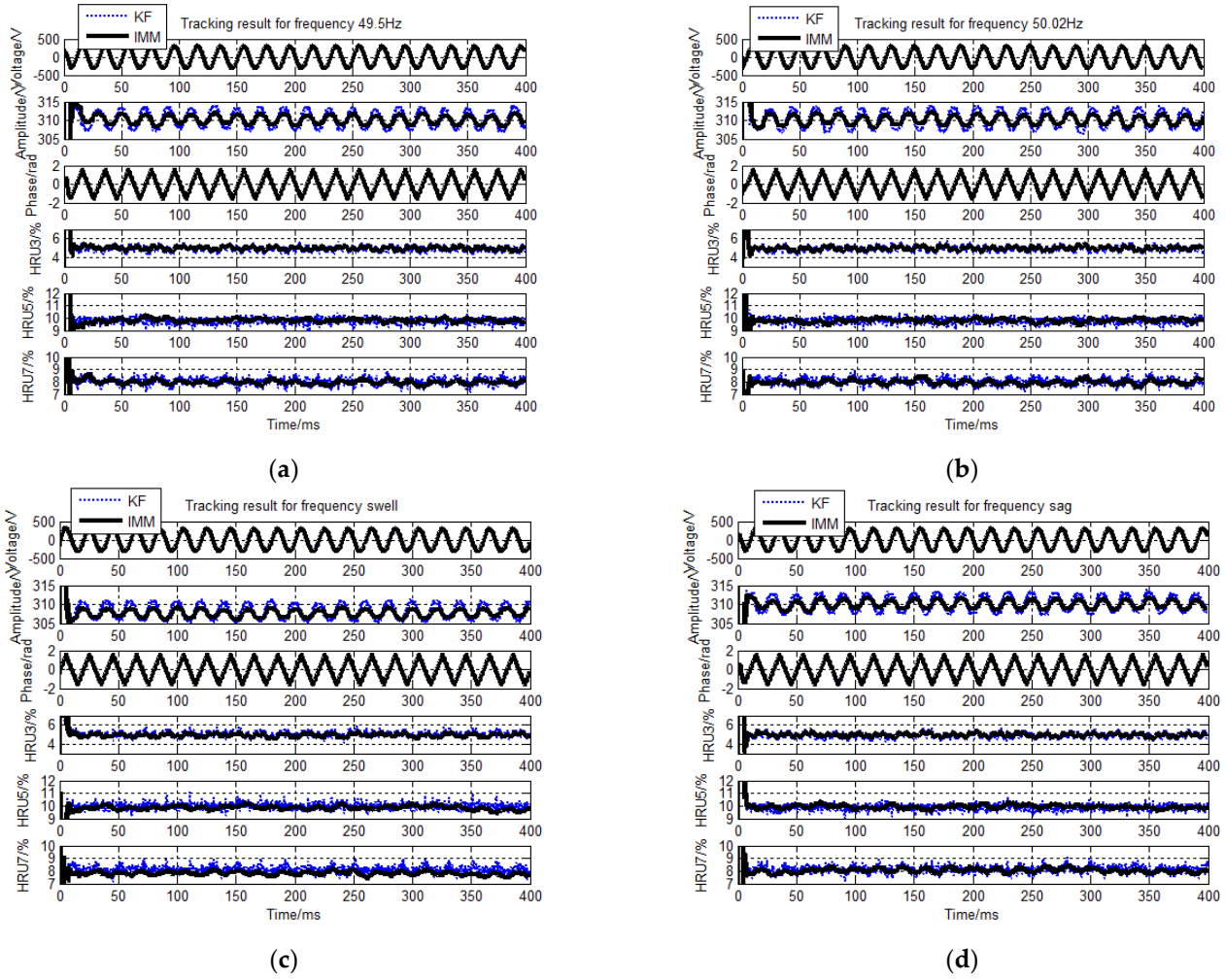

Figure 15. Experiment tracking results for voltage frequency slight fluctuations. (**a**) Experiment tracking results for frequency 49.98 Hz; (**b**) Experiment tracking results for frequency 50.02 Hz; (**c**) Experiment tracking results for frequency swell; (**d**) Experiment tracking results for frequency sag.

6. Conclusions

This paper newly presents the IMM algorithm to track the fundamental and harmonic components of the AC voltage signal under grid frequency fluctuation conditions. First of all, the orthogonal vector dynamic (OVD) model is re-derived from the stochastic process theory, which made it clear that the covariance matrix is related to the sampling cycle. Then, the IMM algorithm based on the two OVD models (OVD-IMM) is proposed. The advantage of the proposed OV-IMM algorithm is that it does not require the signal frequency detection and feedback like conventional tracking algorithms. In this paper, we simulate by two kinds of scenario data separately, which are (a) voltage frequency heavy fluctuations and (b) voltage frequency slight fluctuations. The experiment applies the same scenario data as the simulation. The results show that the fundamental and harmonic components tracking accuracy of IMM algorithm is higher than single model algorithm. Both the fundamental and harmonic components, the proposed OVD-IMM algorithm is stable and accurate, and is not affected by grid frequency fluctuations. In the future, it would be employed in some real world applications, such as synchronous control in power system [43].

Author Contributions: Conceptualization, H.N. and X.N.; methodology, H.N. and X.N.; software, H.N.; validation, H.N. and X.N.; formal analysis, H.N.; investigation, H.N.; resources, H.N.; data curation, H.N.; writing—original draft preparation, H.N.; writing—review and editing, H.N.; visual-

ization, H.N.; supervision, X.N.; project administration, X.N.; funding acquisition, X.N. All authors have read and agreed to the published version of the manuscript.

Funding: This research was funded by National Natural Science Foundations of China, grant number 51867017 "Research on Power Quality Dynamic Tracking and Real-time Detection Method for Microgrid Complex Source Load Environment".

Conflicts of Interest: The authors declare no conflict of interest.

References

1. Auger, F.; Hilairet, M.; Guerrero, J.M.; Monmassonet, E.; Orlowska-Kowalska, T.; Katsura, S. Industrial Applications of the Kalman Filter: A Review. *IEEE Trans. Ind. Electron.* **2013**, *60*, 5458–5471. [CrossRef]
2. Enayati, J.; Moravej, Z. Real-time harmonic estimation using a novel hybrid technique for embedded system implementation. *Int. Trans. Electr. Energy Syst.* **2017**, *27*, e2428. [CrossRef]
3. Enayati, J.; Moravej, Z. Real-time harmonics estimation in power systems using a novel hybrid algorithm. *IET Gener. Transm. Distrib.* **2017**, *14*, 3532–3538. [CrossRef]
4. Xu, W.; Huang, C.; Xie, X. Analysis and Application of Taylor-Kalman Filters under a Distorted Grid Condition. *IEEE Access* **2020**, *8*, 106822–106831. [CrossRef]
5. Chenchen, W.; Magaña, M.E.; Cotilla-Sánchez, E. Dynamic Frequency and Amplitude Estimation for Three-Phase Unbalanced Power Systems using the Unscented Kalman Filter. *IEEE Trans. Ins. Meas.* **2019**, *68*, 3387–3395.
6. Nie, X. Detection of Grid Voltage Fundamental and Harmonic Components Using Kalman Filter Based on Dynamic Tracking Model. *IEEE Trans. Ind. Electron.* **2020**, *67*, 1191–1200. [CrossRef]
7. Kanieski, J.M.; Tambara, R.V.; Pinheiro, H. Real-Time Detection of Interharmonics and Harmonics of AC Electric Arc Furnaces on GPU Framework. *IEEE Trans. Indu. Appl.* **2019**, *55*, 1373–1378.
8. Xi, Y.; Tang, X.; Li, Z.; Cui, Y.; Zhao, T.; Zeng, X.; Guo, J.; Duan, W. Harmonic estimation in power systems using an optimised adaptive Kalman filter based on PSO-GA. *IET Gener. Transm. Distrib.* **2019**, *13*, 3968–3979. [CrossRef]
9. Xi, Y.; Li, Z.; Zeng, X.; Tang, X.; Zhang, X.; Xiao, H. Fault location based on travelling wave identification using an adaptive extended Kalman filter. *IET Gener. Transm. Distrib.* **2018**, *12*, 1314–1322. [CrossRef]
10. Xi, Y.; Zhang, X.; Li, Z.; Zeng, X.; Tang, X.; Cui, Y.; Xiao, H. Double-ended travelling-wave fault location based on residual analysis using an adaptive EKF. *IET Signal. Process.* **2018**, *12*, 1000–1008. [CrossRef]
11. Alam, S.J.; Arya, S.R. Control of UPQC based on steady state linear Kalman filter for compensation of power quality problems. *Chin. J. Electr. Eng.* **2020**, *6*, 52–65. [CrossRef]
12. Naseri, F.; Kazemi, Z.; Farjah, E.; Ghanbari, T. Fast Detection and Compensation of Current Transformer Saturation Using Extended Kalman Filter. *IEEE Trans. Power Deliv.* **2019**, *34*, 1087–1097. [CrossRef]
13. Ahmed, H.; Biricik, S.; Benbouzid, M. Linear Kalman Filter-Based Grid Synchronization Technique: An Alternative Implementation. *IEEE Trans. Ind. Inform.* **2021**, *17*, 3847–3856. [CrossRef]
14. Samet, H.; Gashtasbi, S.; Tashakor, N.; Ghanbariet, T. Improvement of reactive power calculation in electric arc furnaces utilising Kalman filter. *IET Sci. Meas. Technol.* **2017**, *11*, 241–248. [CrossRef]
15. Zhao, S.; Huang, B.; Liu, F. Linear Optimal Unbiased Filter for Time-Variant Systems without Apriori Information on Initial Conditions. *IEEE Trans. Autom. Control* **2017**, *62*, 882–887. [CrossRef]
16. Sadigh, K.; Smedley, K.M. Fast and precise voltage sag detection method for dynamic voltage restorer (DVR) application. *Electr. Power Syst. Res.* **2016**, *130*, 192–207. [CrossRef]
17. Helena, L.; Liboni, B.; Oliveira, M.C.; Silva, I.N. On the problem of optimal estimation of balanced and symmetric three-phase signals. *Int. J. Electr. Power Energy Syst.* **2017**, *91*, 155–165.
18. Subhra, D.; Sudipta, D. Real-time cross-correlation-based technique for detection and classification of power quality disturbances. *IET Gener. Transm. Distrib.* **2018**, *12*, 1661–1671.
19. Li, J.; Qin, G.; Li, Y.; Ruan, X. Research on power quality disturbance identification and classification technology in high noise back-ground. *IET Gener. Transm. Distrib.* **2019**, *13*, 1661–1671. [CrossRef]
20. Wang, Y.; Raza, A.; Mohammed, F.P.; Ravishankar, J.; Phung, T. Detection and classification of disturbances in the islanded micro-grid by using wavelet transformation and feature extraction algorithm. *J. Eng.* **2019**, *2019*, 5284–5286. [CrossRef]
21. Chakravorti, T.; Patnaik, R.K.; Dash, P.K. Detection and classification of islanding and power quality disturbances in microgrid. *IET Signal Process* **2018**, *12*, 82–94. [CrossRef]
22. Singh, U.; Singh, S.N. Optimal Feature Selection via NSGA-II for Power Quality Disturbances Classification. *IEEE Trans. Ind. Inform.* **2018**, *14*, 2994–3002. [CrossRef]
23. Zhong, T.; Zhang, S.; Cai, G.; Huang, N. Power-quality disturbance recognition based on time-frequency analysis and decision tree. *IET Gener. Transm. Distrib.* **2018**, *12*, 4153–4162. [CrossRef]
24. Yanhui, X.; Zewen, L.; Xiangjun, Z.; Xin, T. Detection of power quality disturbance using an adaptive process noise covariance Kalman filte. *Digit. Signal Process.* **2018**, *76*, 34–49.
25. Markovska, M.; Taskovski, D.; Kokolanski, Z.; Dimchev, V.; Velkovski, B. Real-Time Implementation of Optimized Power Quality Events Classifier. *IEEE Trans. Ind. Appl.* **2020**, *56*, 3431–3442. [CrossRef]

26. Achlerkar, P.D.; Samantaray, S.R.; Sabarimalai Manikandan, M. Variational Mode Decomposition and Decision Tree Based Detection and Classification of Power Quality Disturbances in Grid-Connected Distributed Generation System. *IEEE Trans. Smart Grid.* **2018**, *9*, 3122–3132. [CrossRef]
27. Panigrahi, R.; Subudhi, B.; Panda, P.C. A Robust LQG Servo Control Strategy of Shunt-Active Power Filter for Power Quality Enhancement. *IEEE Trans. Power Electron.* **2016**, *31*, 2860–2869. [CrossRef]
28. Panigrahi, R.; Subudhi, B. Performance enhancement of shunt active power filter using a kalman filter-based H∞ control strategy. *IEEE Trans. Power Electron.* **2017**, *32*, 2622–2630. [CrossRef]
29. Ferrero, R.; Pegoraro, P.A.; Toscani, S. Synchrophasor Estimation for Three-Phase Systems Based on Taylor Extended Kalman Filtering. *Ins. Meas.* **2020**, *69*, 6723–6730. [CrossRef]
30. Golestan, S.; Guerrero, J.M.; Vasquez, J.C.; Abusorrah, A.M.; Al-Turki, Y. Single-Phase FLLs Based on Linear Kalman Filter, Limit-Cycle Oscillator, and Complex Bandpass Filter: Analysis and Comparison with a Standard FLL in Grid Applications. *IEEE Trans. Power Electron.* **2019**, *34*, 1064–1073. [CrossRef]
31. Swain, S.; Subudhi, B. Grid Synchronization of a PV System with Power Quality Disturbances using Unscented Kalman Filtering. *IEEE Trans. Sustain. Energy* **2018**, *10*, 1240–1247. [CrossRef]
32. Xu, W.; Huang, C.; Jiang, H. Analyses and Enhancement of Linear Kalman-Filter-Based Phase-Locked Loop. *IEEE Trans. Instrum. Meas.* **2021**, *70*, 6504510. [CrossRef]
33. Golestan, S.; Guerrero, J.M.; Vasquez, J.C. Steady-State Linear Kalman Filter-Based PLLs for Power Applications: A Second Look. *IEEE Trans. Ind. Electron.* **2018**, *65*, 9795–9800. [CrossRef]
34. Schäfer, B.; Beck, C.; Aihara, K.; Witthaut, D.; Timme, M. Non-Gaussian power grid frequency fluctuations characterized by Lévy-stable laws and superstatistics. *Nat. Energy* **2018**, *3*, 119–126. [CrossRef]
35. Blom, H.A.P.; Bar-Shalom, Y. The interacting multiple model algorithmfor systems with Markovian switching coefficients. *IEEE Trans. Autom. Control* **1988**, *33*, 780–783. [CrossRef]
36. Hwang, I.; Seah, C.E.; Lee, S. A Study on Stability of the Interacting Multiple Model Algorithm. *IEEE Trans. Autom. Control* **2016**, *62*, 901–906. [CrossRef]
37. Lim, J.; Kim, H.-S.; Park, H.-M. Interactive-Multiple-Model Algorithm Based on Minimax Particle Filtering. *IEEE Signal Process. Lett.* **2019**, *27*, 36–40. [CrossRef]
38. Lin, H.; Lam, J.; Chen, M.Z.Q.; Shu, Z.; Wu, Z.-G. Interacting Multiple Model Estimator for Networked Control Systems: Stability, Convergence, and Performance. *IEEE Trans. Autom. Control* **2019**, *64*, 928–943. [CrossRef]
39. Ma, J.; Guo, X. Combination of IMM Algorithm and ASTRWCKF for Maneuvering Target Tracking. *IEEE Access* **2020**, *8*, 143095–143103. [CrossRef]
40. He, H.; Liu, G.; Zhu, X.; He, L.; Tian, G. Interacting Multiple Model-Based Human Pose Estimation Using a Distributed 3D Camera Network. *IEEE Sens. J.* **2019**, *19*, 10584–10590. [CrossRef]
41. Kong, X.; Zhang, X.; Zhang, X.; Wang, C.; Chiang, H.-D.; Li, P. Adaptive Dynamic State Estimation of Distribution Network Based on Interacting Multiple Model. *IEEE Trans. Sustain. Energy* **2021**, 1. [CrossRef]
42. Brown, R.G.; Hwang, P.Y.C. *Introduction to Random Signals and Applied Kalman Filtering with MATLAB Exercises*, 4th ed.; John Wiley& Sons, Inc.: Hoboken, NJ, USA, 2011.
43. Zografos, D.; Ghandhari, M. Power system inertia estimation by approaching load power change after a disturbance. In Proceedings of the 2017 IEEE Power & Energy Society General Meeting, Chicago, IL, USA, 16–20 July 2017; pp. 1–5.